



Deposited via The University of Sheffield.

White Rose Research Online URL for this paper:

<https://eprints.whiterose.ac.uk/id/eprint/209205/>

Version: Published Version

---

**Article:**

Goodall, A.D., Yiannakou, G., Chechik, L. et al. (2023) Geometrical control of eddy currents in additively manufactured Fe-Si. *Materials & Design*, 230. 112002. ISSN: 0264-1275

<https://doi.org/10.1016/j.matdes.2023.112002>

---

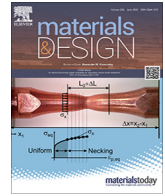
**Reuse**

This article is distributed under the terms of the Creative Commons Attribution (CC BY) licence. This licence allows you to distribute, remix, tweak, and build upon the work, even commercially, as long as you credit the authors for the original work. More information and the full terms of the licence here:

<https://creativecommons.org/licenses/>

**Takedown**

If you consider content in White Rose Research Online to be in breach of UK law, please notify us by emailing [eprints@whiterose.ac.uk](mailto:eprints@whiterose.ac.uk) including the URL of the record and the reason for the withdrawal request.



# Geometrical control of eddy currents in additively manufactured Fe-Si

Alexander D. Goodall<sup>a,\*</sup>, Georgios Yiannakou<sup>b</sup>, Lova Chechik<sup>a</sup>, Ria L. Mitchell<sup>a</sup>, Geraint W Jewell<sup>b</sup>, Iain Todd<sup>a</sup>

<sup>a</sup> Department of Materials Science and Engineering, University of Sheffield, Sheffield, UK

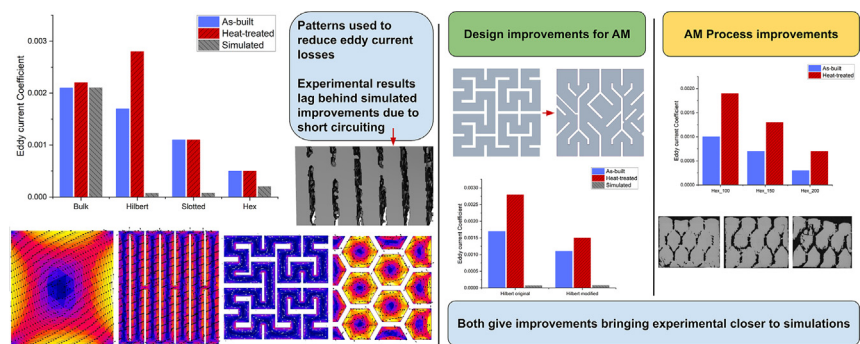
<sup>b</sup> Department of Electronic and Electrical Engineering, University of Sheffield, Sheffield, UK



## HIGHLIGHTS

- Simulations shown to match experimental losses in solid cross-section of Fe-6.5 wt%Si.
- Air gaps in the cross section are used to improve eddy current losses, introducing a novel hexagonal cross section.
- Experimental samples underperform when compared to simulated losses.
- XCT shows reduced electrical short-circuiting from 27% to 0.5%, bringing sample losses closer to simulated values.

## GRAPHICAL ABSTRACT



## ARTICLE INFO

### Article history:

Received 24 February 2023

Revised 27 April 2023

Accepted 12 May 2023

Available online 13 May 2023

### Keywords:

Soft magnetic material

Eddy current loss

Fe-Si

Electric machine

Magnetic characterisation

## ABSTRACT

Additive manufacturing has enabled the processing of high silicon electrical steels which have excellent soft magnetic properties. In bulk form, core losses as a result of eddy currents would be too large to allow their use in high-frequency electrical machines, therefore strategies are needed to reduce eddy currents. Additive manufacturing affords high part complexity and provides the opportunity for cross sectional patterns within the material to limit eddy current generation. This study investigates several designs, including a novel hexagonal pattern which is shown to have the lowest eddy current loss coefficient of 0.0005, less than 25% of the bulk material which has an eddy current loss coefficient of 0.0021. Heat treatment is shown to increase the eddy current losses, demonstrating that for high-frequency machines, it may be beneficial to use the material in the as-built state. Physical samples were compared to their intended geometries, showing there are defects in these complex cross sections causing increased eddy currents when compared to simulations, but that geometrical accuracy can be improved by alternative design methodology which experimentally experiences smaller losses. These novel cross sectional designs may be implemented into an electric machine that has a 3D magnetic flux pathway enabled by additive manufacturing, affording more flexibility for electrical engineers to design new motor architectures in the pursuit of higher power density machines.

Crown Copyright © 2023 Published by Elsevier Ltd. This is an open access article under the CC BY license (<http://creativecommons.org/licenses/by/4.0/>).

*Abbreviations:* AB, as-built; HT, heat-treated; L-PBF, laser - powder bed fusion; EM, electric machine; SF, stacking factor.

\* Corresponding author.

E-mail address: [adgoodall1@sheffield.ac.uk](mailto:adgoodall1@sheffield.ac.uk) (A.D. Goodall).

<https://doi.org/10.1016/j.matdes.2023.112002>

0264-1275/Crown Copyright © 2023 Published by Elsevier Ltd.

This is an open access article under the CC BY license (<http://creativecommons.org/licenses/by/4.0/>).

## 1. Introduction

Electric motors are one of the most widely used electric machines (EM), accounting for approximately 50% of energy consumption in industry [1]. As part of a global drive to improve efficiency and reduce energy consumption, research efforts are

being made to improve the performance of EMs, with high power density, fault-tolerant and efficient machines for aerospace being a major research focus [2].

Additive manufacturing (AM) has the ability to manufacture parts with complex 3D geometry due to the layer-by-layer process. This technology could enable novel architectures for electric motors to give higher torque density, lighter mass, and other benefits [3,4]. AM has been used to process both soft magnetic materials [5] and copper [6], which are key materials to enable the effective design of electric motors. However, to fully exploit the advantages afforded by AM, these materials must first be characterised and then implemented using design strategies that capitalise on the advantages of AM.

Electrical steels (Fe-Si) are used extensively in soft magnetic applications due to their high saturation, permeability, and relatively high electrical resistance. Fe-6.5 wt% Si has been shown to exhibit some of the best properties for soft magnets [7,8], however Fe-3 wt% Si is more frequently used due to its workability with conventional processes [9]. Stacked laminate sheets with a thin layer of insulation between layers are the most common approach to creating soft magnetic cores. By electrically isolating the layers, eddy current losses are greatly reduced, but this limits design freedom to two-dimensional systems due to the difficulty of building 3D shapes from thin sheets. AM and specifically laser powder bed fusion (L-PBF) is capable of building complex 3D shapes from high silicon steels [10,11] and other soft magnetic materials [12,13], offering the geometrical freedom to manipulate both magnetic flux pathways and eddy current flows. Just as electrical steel laminations are used over bulk electrical steel, when utilising soft magnetic materials in AM, strategies must be used to limit the eddy current generation. As shown by Goll [10], Plotkowski [11], and Tiismus [14], features may be designed into the cross section of the material to reduce the generated eddy currents by forcing them to experience a longer, more resistive path. The most complex of these is the Hilbert pattern [11], which has been demonstrated in 2.5D, with a constant cross section in the build plane. To capitalise on the geometrical freedom of AM, flux pathways must be able to run in three-dimensional space, otherwise, electrical steel laminations would likely experience lower losses at a lower cost. This study will only focus on complex cross sections which could be produced at any angle in the build chamber. The ability to improve upon one or more properties of EMs by using AM has been demonstrated [15]. Attempts have been made to characterise soft magnetic materials built using L-PBF [10,11,16–22], however, in AM, the processing parameters can affect the magnetic properties important for EM design.

This paper gives an overview of the magnetic properties of L-PBF built Fe-6.5 wt% Si in the as-built (AB) and heat treated (HT) conditions. Simulations assess the eddy current losses in several cross sections, designed to capitalise on the geometrical freedom of AM to reduce eddy current losses. These cross sections are tested experimentally at a range of frequencies between 5 and 1000 Hz, identifying the eddy current coefficient and quantifying the improvement that can be gained over the bulk. The cross sections are critically analysed to investigate physical geometry compared to modelled geometry. This paper demonstrates how the losses in an additively manufactured EM core could be managed to enable three-dimensional magnetic circuits.

## 2. Experimental methods

### 2.1. Sample processing

Spherical high silicon steel powder (Fe-6.5 wt% Si) supplied by Höganäs AB was used for all samples in this paper. The particle size

and chemical composition as stated by the supplier are in Table 1, demonstrating a lower silicon content at 6.2 wt%. Powder composition can vary between batches and therefore this lower silicon content will still be referred to as Fe-6.5 wt% Si to allow easy comparison with other works in literature, as 6.5 wt% Si is the most commonly used high silicon electrical steel.

This powder was processed using an AconityMINI from Aconity3D GmbH. This is a L-PBF machine that uses a 200 W ytterbium-doped continuous laser with a spot size of 70 µm. During each layer, the laser scans over the cross sectional area, melting the material which solidifies creating the desired object (Fig. 1). The layer rotation angle ( $\theta$ ) was 67° between each layer. This process is completed under an argon atmosphere with an oxygen content of less than 100 ppm. The samples were built onto a stainless-steel build platform of 140 mm diameter with a constant layer thickness ( $l$ ) of 30 µm. Hatch spacing ( $h$ ), laser power ( $Q$ ), and laser velocity ( $v$ ) were all manipulated during this study. The samples with complex cross sections were built using  $Q = 140$  W,  $v = 0.7$  m/s, and  $h = 70$  µm. All samples were removed from the build platform by wire electrical discharge machining.

5 mm cubic samples were initially built to understand how the laser parameters affect density, cracking, and microstructure. The volumetric energy density (VED), shown in Equation (1), was varied between 37 and 115 J/mm<sup>3</sup> by using a two-level central composite design of experiments, varying the values of  $1/h$  and  $Q/vl$ . Where  $Q$  = laser power,  $v$  = scan speed,  $l$  = layer height, and  $h$  = hatch spacing. These values centred around successful parameters reported in literature shown to produce high density parts from additively manufactured high silicon steel [10,16]. The parameters used are given in Table 2.

$$VED = \frac{Q}{vlh} \quad (1)$$

### 2.2. Metallographic and magnetic characterisation

Cubes were sectioned along the build plane and build direction (Fig. 1) and prepared for microscopy using standard metallurgical techniques. An Olympus BX51 microscope was used in conjunction with the Clemex Vision PE system to obtain optical micrographs, followed by analysis using ImageJ [23] to determine the density. The density measurement was repeated 5 times by cropping the image into 5 separate areas, and standard error was calculated using Equation (2), where SE is standard error,  $\sigma$  is the standard deviation and  $n$  is the number of samples.

$$SE = \frac{\sigma}{\sqrt{n}} \quad (2)$$

Magnetic properties were characterised by testing a toroidal sample with a rectangular cross section, using an AMH-1 K Permeameter by Laboratorio Elettrofisico. The dimensions of the toroid were approximately 30/38 mm inner/outer diameter and 4.5 mm thickness, with each sample being measured accurately with a digital caliper. This was chosen to respect the sample dimensions in BS 60404-6:2018 [24]. The secondary search coil used 0.35 mm single-core insulated copper wire with 45 turns, whereas the primary driving coil used 1.5 mm multi-core insulated copper wire with 40 turns. DC normal magnetisation curves were used to obtain the maximum relative permeability ( $\mu_{max}$ ). Coercive force ( $H_c$ ) was measured using a quasi-static B-H loop to allow direct comparison with the literature. AC power losses were obtained from B-H loops measured at various frequencies between 5 and 1000 Hz. For the complex cross section samples, a full ring was used for magnetic characterisation, and one quarter of a ring was used to analyse the cross section and stacking factor (SF) with optical microscopy. SF is the volume of material/ total volume

**Table 1**  
Fe-6.5 wt Si powder details.

Chemical Composition (wt%)	Size Distribution ( $\mu\text{m}$ )								
Iron	Silicon	Oxygen	Nitrogen	Carbon	Sulphur	X10	X50	X90	X99
93.735	6.200	0.036	0.016	0.01	0.003	15.67	25.72	42.07	57.23

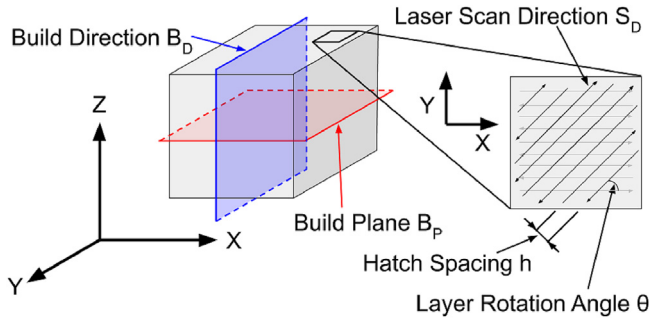


**Fig. 1.** Parameters relating to L-PBF sample processing showing build plane and build direction, laser scan direction, hatch spacing, and layer rotation angle.

including insulation, which in this study is air gaps. Power losses during magnetic cycling can be described by Equation (3) [25]. Where  $P_{\text{loss}}$  is the total power loss,  $f$  is the frequency,  $B_m$  is the flux density which is 1 T for this study,  $\rho$  is the resistivity of the material,  $t$  is the thickness of the material,  $C_0$  &  $C_1$  are constants,  $P_h$ ,  $P_{EC}$  &  $P_{Ex}$  are hysteresis power loss, eddy current power loss and excess power loss respectively. This equation only applies to solid material and hence the  $\frac{\pi^2 t^2}{6\rho}$  term can be replaced with a constant for this study,  $C_{\text{eddy}}$ , which will express the benefit of the cross sectional designs. The inclusion of  $C_1$  did not improve the fitting of the data and was set to 0 for this study. Hence the power losses in this study are described by Equation (4), with energy loss per cycle ( $E_{\text{cycle}}$ ) described in Equation (5).

$$P_{\text{loss}} = C_0 B_m^2 f + \frac{\pi^2 t^2}{6\rho} (B_m f)^2 + C_1 B_m f^{1.5} = P_h + P_{EC} + P_{Ex} \quad (3)$$

$$P_{\text{loss}} = P_h + P_{EC} = C_{\text{hysteresis}} f + C_{\text{eddy}} f^2 \quad (4)$$

$$E_{\text{cycle}} = C_{\text{hysteresis}} + C_{\text{eddy}} f \quad (5)$$

AC measurements were taken at several frequencies. By plotting energy loss per cycle vs frequency, and using a linear fit, the hysteresis ( $C_{\text{hysteresis}}$ ) and eddy current loss coefficients ( $C_{\text{eddy}}$ ) can be obtained, as demonstrated in Fig. 8.

HT (heat treatment) of toroidal samples was performed in a tube furnace under an inert argon atmosphere using the best HT

**Table 2**  
Laser parameters selected using two level central composite DoE.

Laser Power Q (W)	Laser speed v (mm/s)	Hatch spacing h ( $\mu\text{m}$ )	Q/vl (Ws/mm <sup>2</sup> )	1/h (mm <sup>-1</sup> )	VED (J/mm <sup>3</sup> )
145.00	1200.00	100.00	4.03	10.00	40.28
170.00	700.00	100.00	8.10	10.00	80.95
145.00	1200.00	70.00	4.03	14.29	57.54
170.00	700.00	70.00	8.10	14.29	115.65
80.00	850.00	85.00	3.14	11.76	36.91
175.00	650.00	85.00	8.97	11.76	105.58
160.00	900.00	110.00	5.93	9.09	53.87
160.00	900.00	65.00	5.93	15.38	91.17
160.00	900.00	85.00	5.93	11.76	69.72
180.00	1000.00	85.00	6.00	11.76	70.59
140.00	780.00	85.00	5.98	11.76	70.39
100.00	550.00	85.00	6.06	11.76	71.30
60.00	300.00	85.00	6.67	11.76	78.43

regime identified by Garibaldi [26], 1150 °C for one hour, followed by furnace cooling to room temperature.

Toroidal samples with a complex cross section such as the hexagonal section are built with the cross section running circumferentially around the toroid. The Hilbert and slotted toroid's were built without supporting structures, however the hexagonal cross section toroid had periodic support structures built as per Fig. 2, which enables the hexagons to be connected without having more than two connected at any one point, keeping the cross sectional area low.

### 2.3. Electromagnetic simulation

To observe and compare eddy current generation and flow inside the complex cross sections and bulk material, multi-physics electromagnetic simulations were performed using a steady-state AC model in Altair Flux. A model was set up to mimic the physical toroid using the same geometrical dimensions and number of turns in the primary coil. 1/40th (1 turn on the primary coil) of the system was simulated due to the symmetry of the system and to reduce the computational demand. Non-meshed coils were used, whilst the mesh was created with the aided mesh generator. The modelled electric circuit consists of the magnetisation winding connected to a sinusoidally driven current source of frequency 50 Hz. The amplitude of the current was varied to reach an average flux density value of 1 T, as measured by a radial-section cut-plane through the material. The measured joule losses ( $P_{ec}$ ) were then divided by  $f^2$  to give  $C_{\text{eddy}}$  (Equation (2)). It was confirmed that  $C_{\text{eddy}}$  was independent of frequency in the simulations by running the bulk cross section at several frequencies between 5 and 1000 Hz. The material properties used are taken from the measurements of the bulk sample, and were inputted as type – “isotropic analytic saturation” (arctg, 2coef), with an initial relative permeability of 10,000, saturation magnetisation of 1.5 T, with electrical resistivity set as “spatial isotropic resistivity” of  $8.2 \times 10^{-7}$  Ohm.m. An example of the model for the bulk cross section is shown in Fig. 3.

### 2.4. X-ray computed tomography (XCT) and analysis

A toroidal sample was mounted on a sample holder and scanned using a Zeiss Xradia 620 Versa X-ray microscope (XRM). X-rays were generated from a tungsten transmission target and

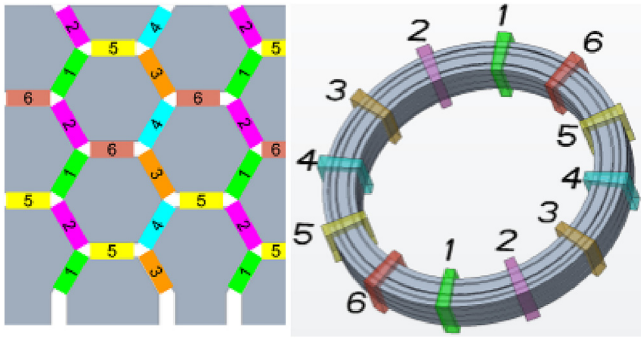


**Fig. 2.** Hexagonal cross section support structures which are periodically placed every  $30^\circ$  around the ring. At each of these locations two of the hexagons are connected as per the diagram cross section schematic (left).

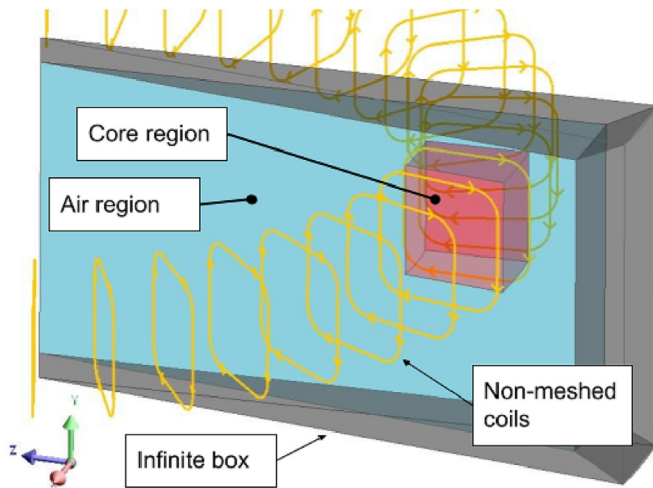


**Fig. 3.** Altair flux 3D model used to simulate eddy current losses in toroidal samples, showing the different volume regions and the coils and symmetry used.

collected on a CCD (charge-coupled device) 16-bit  $2000 \times 2000$  pixel detector. Approximately  $\frac{1}{4}$  of the ring was scanned, achieving a voxel (isotropic 3D pixel) resolution of  $16.7 \mu\text{m}$ . A filter (HE6) was inserted to reduce unwanted lower energy X-rays. 1601 projection images were collected per sample, and a 2-second exposure time was applied to improve the signal-to-noise ratio. A filtered back projection method was used to reconstruct the data, and reconstructed.txm volumes were converted to 8-bit greyscale image stacks (.tiff) using Zeiss Reconstructor software.

Tiff images were orientated to view the build plane (XY) to give a consistent cross sectional pattern for the slotted sample. Using ImageJ [23], an area of  $7 \times 5 \text{ mm}$  was cropped for analysis, and the image was binarised by thresholding. By summing the width of all the short circuit connections in each air gap and dividing

by the total length of the air gap in the image, a % of electrical shorting can be measured (Fig. 4) which represents the percentage of area connected through the air gap. Through the sample, ten images with  $160 \mu\text{m}$  interval between them were analysed for short-circuiting and the results averaged. For the hexagonal samples, nine images were used, three from each of the vertical sides of the hexagons from each row, with an interval of  $100 \mu\text{m}$ .

### 3. Results and discussion

#### 3.1. Bulk processing and magnetic characterisation

5 mm cubes were used to assess the processing window for Fe-6.5 wt% Si. For all samples, the density in the build plane was higher than the build direction, therefore the results shown are from the build direction to give a conservative approach. Lower energy density led to a lack of fusion defects and low density (Fig. 5b), whilst high energy density introduces cracking and key-hole porosity (Fig. 5d). The best parameters found to give a density of over 99.5% were  $Q = 170 \text{ W}$ ,  $v = 0.7 \text{ m/s}$ , and  $h = 70 \mu\text{m}$ . This set of parameters has been used for all subsequent samples.

The thermal conditions during the build process for the toroidal samples are different from that of the cube despite the cross sectional area being similar. The inter-layer time will be increased in the complex cross sections, and the heat transfer out of the component will be changed due to the thinner walls, surrounded by powder which will act as an insulator when compared with bulk material. These differing thermal conditions may impact the microstructure and density of the toroidal samples compared to that of the cubes.

The magnetic properties of the bulk material were measured in both AB and HT conditions. The coercive force was  $143 \text{ A/m}$  in the AB condition, which was reduced to  $26 \text{ A/m}$  for the HT sample. The maximum permeability achieved in this paper is 9,800 for the HT sample, significantly lower than Tiismus et al. who achieved 28,900 [14], and Goll et al. who achieved 31,000 [10]. Consequently, there could be an improvement of the material properties in the bulk condition from those obtained in this study, as factors such as density, grain size, and surface finish could be optimised to yield an improvement, but are outside the scope of this work.

The BH loops at 1 T for frequencies of 5 Hz and 1000 Hz are shown in Fig. 6, demonstrating a large reduction in losses (BH loop area) with HT at 5 Hz, but an increase at 1000 Hz. Losses were measured at a variety of frequencies as illustrated in Fig. 7, showing that at low frequencies the HT sample outperforms the AB sample, whereas, at high frequencies this is reversed. The losses cannot demonstrate the full picture however as the shape of the BH loops in Fig. 6 show, the knee point is lower, and a higher field is required to obtain the same flux density within the AB toroid, especially at low frequencies.

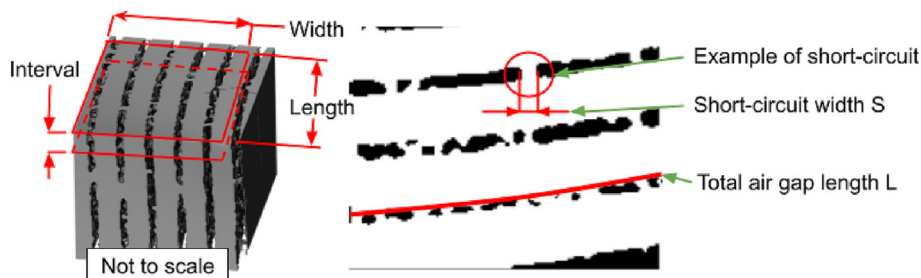


**Fig. 4.** Example of XCT short-circuiting analysis showing the XCT data (left) with the binarized image (right) with an example short-circuit width and total length highlighted. The voxel size attained is  $16.72 \mu\text{m}$  due to the relatively thick sample.

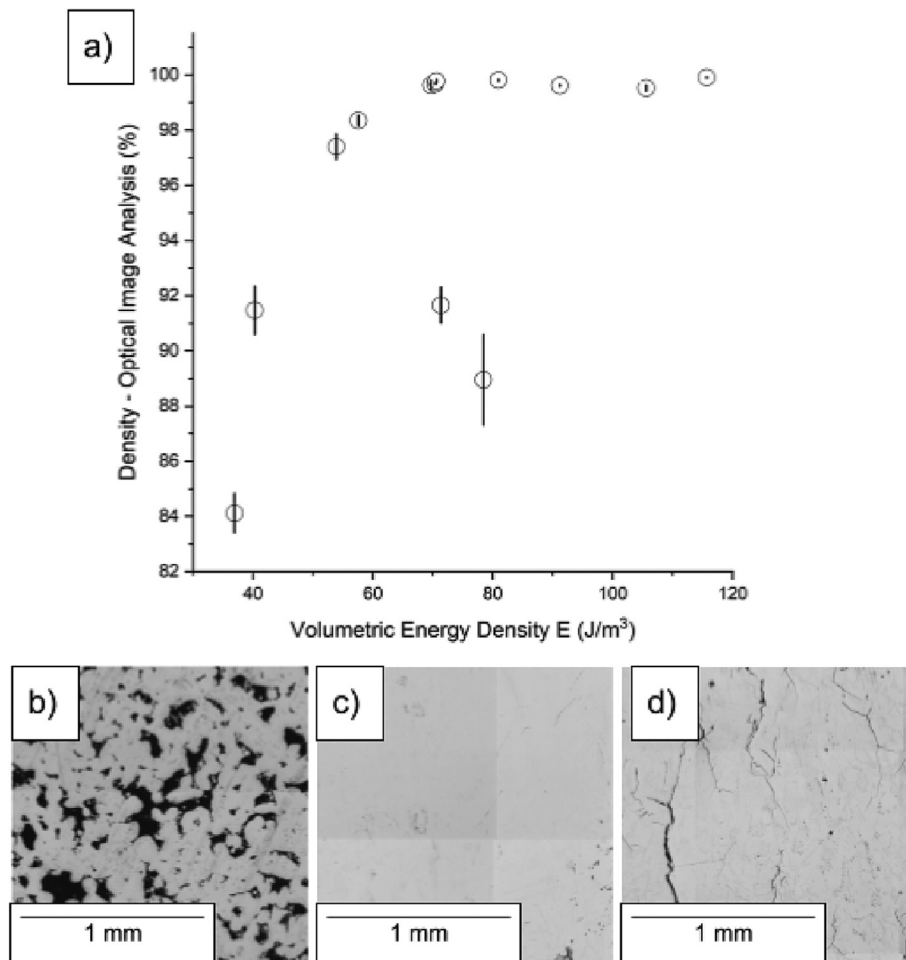


**Fig. 5.** Results showing the effect of changing laser parameters on the density of Fe-Si samples. Error bars show standard error. The samples increase in density up to 70  $J/mm^3$ , whereby increasing energy density does not improve density. There are two outliers with a density below 92% and an energy density of above 70  $J/mm^3$  due to melt pools which have been modelled to be thinner than the hatch spacing. High density was obtained with an energy density of 81  $J/mm^3$  (c). Lack of fusion (b) results from a low energy density of 37  $J/mm^3$ , whereas cracking (d) occurs from a too high energy density of 120  $J/mm^3$ .

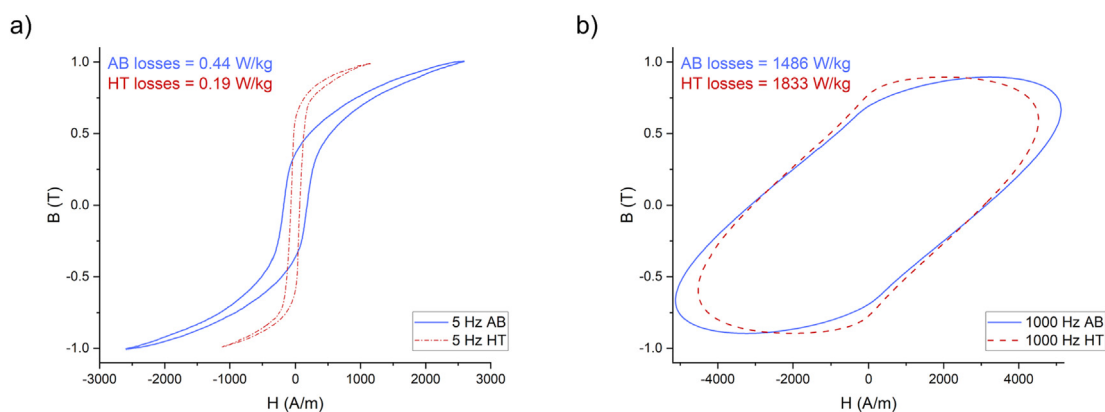


**Fig. 6.** BH loops of the AB and HT condition at 1 T 5 Hz, and 0.9 T 1000 Hz, showing the specific losses (W/kg) demonstrating that HT gives an improvement at 5 Hz but performs worse at 1000 Hz. As this setup can only use a field of 5000 A/m, the 1000 Hz samples were measured at a lower flux density of 0.9 T.

Further work is required to understand the lower losses of the AB sample at high frequency, but it is suspected that the larger grain size of the HT sample is causing an increase in eddy current losses [27]. The losses at higher frequencies are dominated by eddy currents rather than hysteresis losses. Hence, the increased hysteresis losses of the smaller grains in the AB sample, with higher grain boundary density are less impactful than the increased eddy

currents given by the larger grains in the HT sample. As a result of this, the smaller grain size of the AB condition [26], could give a benefit in high-frequency machines.

Fig. 8 shows the data for the linear fit of Equation 5, with an  $R^2$  value of 0.998, demonstrating that it is possible to effectively calculate both  $C_{\text{hysteresis}}$  and  $C_{\text{eddy}}$ . 1000 Hz measurements were excluded from this data set as the eddy currents get very large

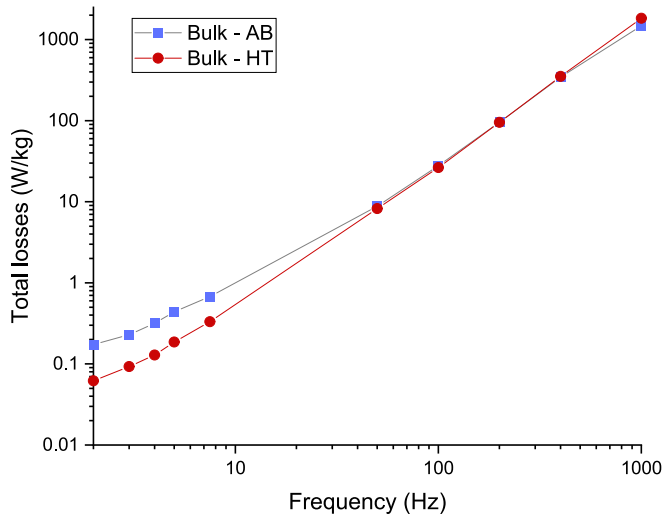


**Fig. 7.** Loss behaviour at a flux density of 1 T for various frequencies, showing that the HT gives an improvement in losses at low frequencies but above 400 Hz, the AB condition demonstrates lower losses. Note: 1000 Hz losses are determined at 0.9 T due to limitations on the maximum field of 5000 A/m.

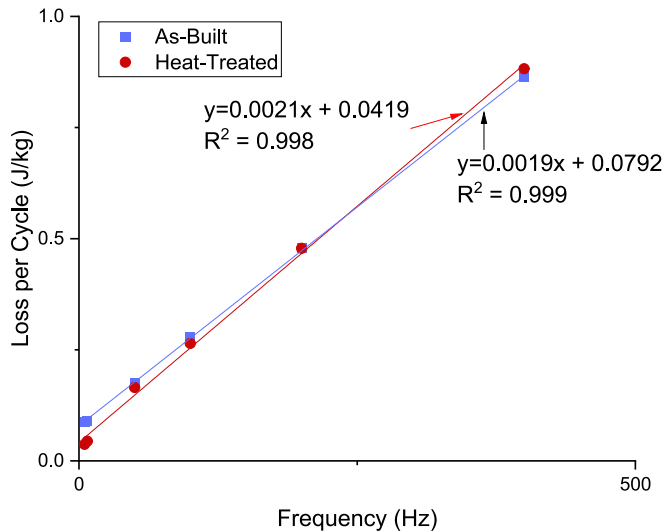


**Fig. 8.** Energy loss per cycle showing that the linear fit can successfully obtain  $C_{eddy}$  and  $C_{hysteresis}$ . Note: 1000 Hz data excluded as loss measurement taken at 0.9 T.

causing a non-linear relationship between frequency and loss per cycle.

### 3.2. Complex cross section eddy current losses

As the power losses at high frequencies are significantly above that of currently available soft magnetic materials, AM of bulk soft magnetic materials will be of little use in high-frequency machines and hence complex cross sections must be implemented to manage the eddy currents. In this study, toroid's with complex cross sections are built using the same parameters as when processing bulk sections, however, the cross sectional area has multiple thin sections ( $\approx 1$  mm). This change in thickness and hence thermal conditions is suspected to have caused porosity in some samples (Fig. 9), highlighting the importance of tailoring parameters for each component or for process control to give a consistent outcome.

To compare several cross sections, electromagnetic simulations were carried out and the eddy current losses were assessed (hysteresis losses are not included). The three best cross sections are shown in this paper, these are the Hilbert pattern first shown in this context by Plotkowski [11], the slotted pattern first shown by Goll (inner slits) [10], and a novel hexagonal design, designed to limit eddy currents to several separated segments. This hexagonal section has periodic (1 mm thick) supporting structures around the toroid which have been omitted from these figures for clarity. These cross sections are shown in Fig. 9. The simulations enable observation of the current flow in the cross section, demonstrating a difference in the method of loss reduction between the slotted and Hilbert patterns, which direct the eddy currents over a longer path when compared to the hexagonal pattern, which contains the eddy currents within a smaller area as shown in Fig. 10 (and in more detail in Appendix 1).

When compared to the bulk cross section throughout the frequency range, the Hilbert and slotted cross sections showed only 4% of the eddy current losses, with the hexagonal cross section showing 10% of the losses. The eddy current coefficients of both the simulated and experimental studies are shown in Fig. 11, demonstrating that the simulations for the bulk cross section have a good correlation to the measured results. The simulations are overly optimistic for the complex cross sections, as although all of these patterns do show an improvement over the bulk material, they do not perform as well as predicted in the simulation. For all the samples it is shown that  $C_{eddy}$  and hence eddy current losses, increase with HT. This is likely due to microstructural changes such as increased grain size and reduced residual stress etc. Hence for high-frequency machines it may be beneficial to not heat treat components, though further study is required to fully understand

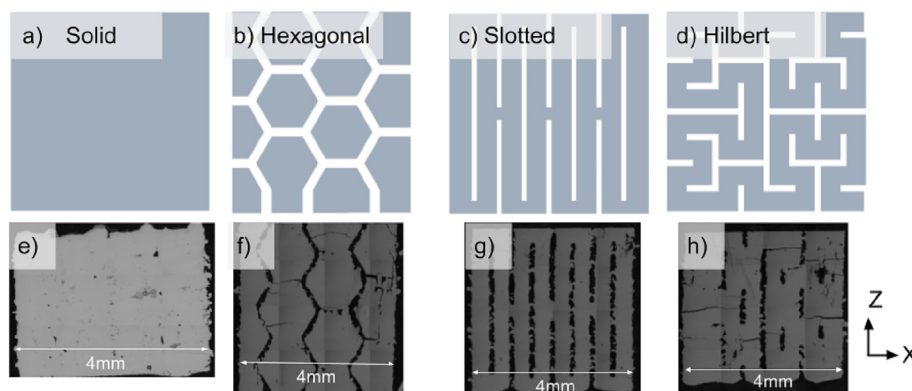


**Fig. 9.** Solid (a,e), Hexagonal (b,f), slotted (c,g), and Hilbert (d,h) cross section showing a micrograph of the AB sample after removal from the baseplate (e,f,g,h), and the cross section as per the design (a,b,c,d). Micrographs show the build direction (Fig. 1).

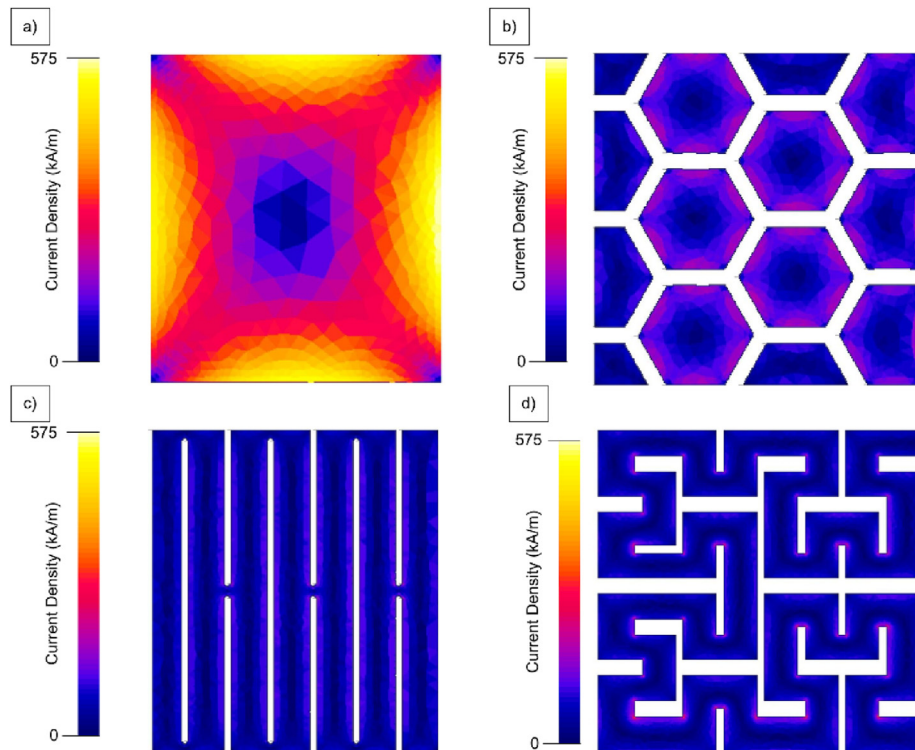


**Fig. 10.** Display of eddy current density inside the bulk section and complex cross sections, demonstrating a clear reduction in eddy current density for all the complex cross sections. This enables the current paths to be observed showing the difference between the hexagonal section which constrains the eddy currents to smaller areas, and the slotted and Hilbert sections which force the currents over longer paths. Full images of each can be found in Appendix 1 including arrows indicating the current flow direction.

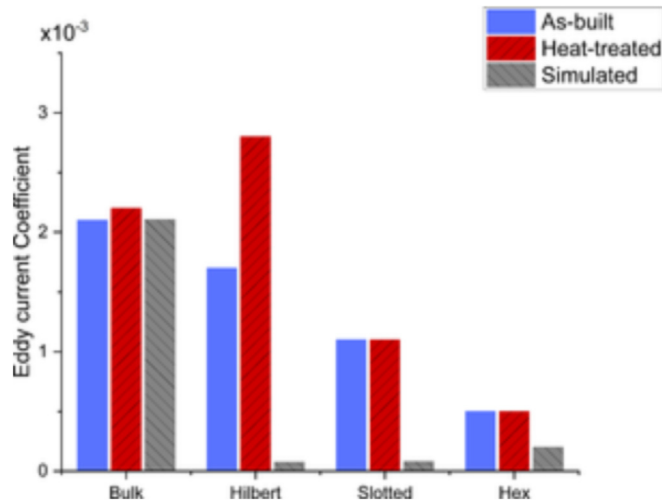


**Fig. 11.** Eddy current losses during electromagnetic simulations of the complex cross sections compared to the bulk cross section, performed at a flux density of 1 T with varying frequencies. All the complex cross sections showed an improvement over the bulk, with the hexagonal cross section showing the lowest losses at approximately 6% of the losses of the bulk cross section.

this. To be used in an EM, there are other important material performance parameters to inspect such as permeability, saturation, and BH loop shape. Fig. 12 demonstrates a qualitative comparison of the BH loops for the best performing cross section which is hexagonal, the area of the BH loop is smaller, showing the decrease in losses, however, the permeability is lower meaning that a machine would require a higher field to obtain the same flux density.

Simulations such as those above could allow for design optimisation. By modifying the size of the hexagons based on their loca-

tion, with larger hexagons at the centre and smaller hexagons at the edge where the eddy currents are higher, or differing hexagon sizes based on the intended frequency of operation losses may be reduced. The cross sections used in the simulation also assume that the pattern is accurately resolved in the AM process, however, Fig. 9 shows that in the experimental samples there are errors in the resolution of the desired design, with shorting between areas that should be electrically isolated, cracking and porosity.

As there is such a disparity between the simulated values and the measured values of  $C_{eddy}$  for the complex cross sections, further investigation into the slotted sample was undertaken as this was the simplest geometry. Fig. 13 shows a micrograph of the slotted cross section, demonstrating some issues in the resolution of the desired geometry. Firstly, there are large pores that have the morphology of lack of fusion defects. This could be caused by using the same parameters for a 5 mm thick cross section and a 0.5 mm thick cross section which will have different thermal conditions. There is also some cracking apparent, which could be caused by the sharp changes in geometry giving rise to stress concentrations whilst cooling. There is also a possibility that this cracking occurred during hot mounting. However, the most important issue is surface roughness, which causes unwanted electrical contact between areas that should be isolated, termed shorting. This gives pathways for eddy currents to circulate which are not intended in the design of the geometry.

To quantify the amount of shorting between areas that should be separated, XCT was used to give a three-dimensional representation of the component (Fig. 4). The XCT data achieved a voxel size of 16.72  $\mu\text{m}$ , due to the sample thickness. This gives sufficient resolution to see defects that are causing connections. It was found that throughout the slotted sample,  $10 \pm 2\%$  of the area was electrically connected. This equated to an increase of  $C_{eddy}$  from the simulated value of  $7.8 \times 10^{-5}$  to  $110 \times 10^{-5}$ , over an order of magnitude larger. Therefore, to improve the performance of these cross sec-

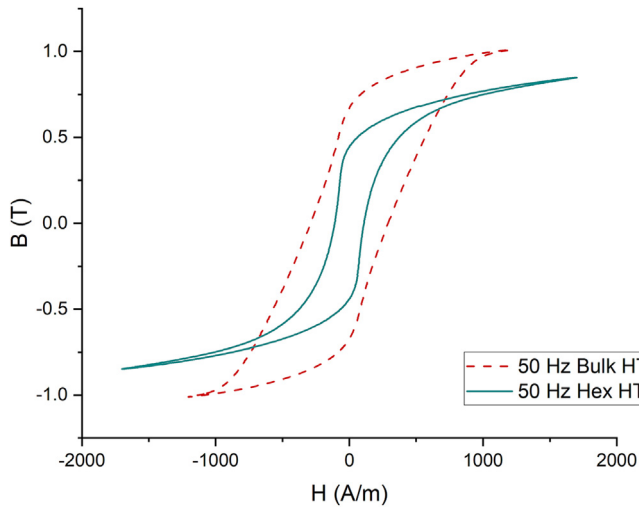


**Fig. 12.** BH loops of bulk and hexagonal cross sections at 50 Hz, showing that although the hexagonal section has significantly lower losses, it requires a larger field to obtain the same flux density. The initial permeability is better for the hexagonal sample however the knee point of the BH loop is at a lower flux density, approximately 0.5–0.6 T rather than 0.7–0.8 T for the bulk cross section.

tions, an improved surface finish would be required, which would reduce electrical shorting, providing large gains as shown by the disparity between simulated and experimental results. There are multiple ways of doing this, such as optimising contour parameters during the process or post processing operations such as electro-polishing.

### 3.3. Cross section design and stacking factor

Further to the surface roughness, improvements in cross sectional resolution can be obtained by the design of the cross section. Although it can be possible to build unsupported horizontal sur-

faces for short distances, in general this is avoided in AM. Hence, the Hilbert cross section used throughout this study is unsuitable for use in any other plane than the build plane (XY plane), as demonstrated by how poorly the physical sample (Fig. 14c) resembles the intended design (Fig. 14a). To ensure 3D flux pathway capability, other designs are necessary which can be built in any orientation. Fig. 14b shows a modified Hilbert cross section, designed to enable building in any orientation in L-PBF by reducing overhanging surfaces to less than 45° overhang, which has been built in the build direction (Fig. 14d). This section shows an improvement and demonstrates the cross section is almost as per the design but would require need further optimisation to be identical. The modified Hilbert cross section shows a higher  $C_{eddy}$  in simulations, however, the physical sample demonstrates an improvement with a lower  $C_{eddy}$  than the original Hilbert cross section (Fig. 14e). To further improve these cross sections, a tool to optimise the topography based upon electromagnetic simulations with manufacturing constraints considered is needed. This would enable the optimum design to be found which would likely be both machine and location (within the machine) specific. Garibaldi et al. [28] attempted topology optimisation for soft magnetics, considering both mechanical stress and magnetics to reduce the weight of a rotor, however, this does not take into account eddy current behaviour. In a stator where the mechanical stresses are low, this optimisation would likely be able to ignore mechanical stress whilst optimising for magnetic performance (including losses). By ensuring the printability of the cross section, air gaps can be minimised, therefore increasing the SF.

The SF is an important material selection parameter for soft magnetic cores, with a higher SF meaning there is more magnetic material to give a higher total flux with the same field. Modern electrical steel laminations can obtain SFs upwards of 95%, whereas the complex cross sections shown so far in this paper have SFs of 90%, 86%, and 91% for the hexagonal, slotted, and Hilbert sections respectively. However, all these cross sections show errors in the resolution of the intended design (Fig. 13).

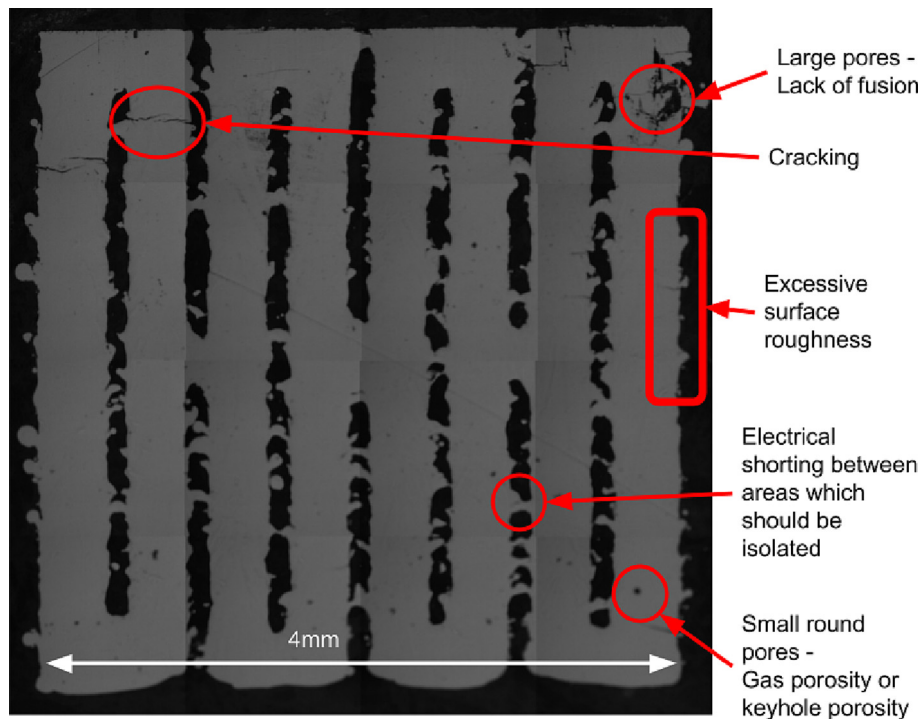


**Fig. 13.** Errors in the resolution of cross section such as shorting, missing air gaps, or cracking/porosity.

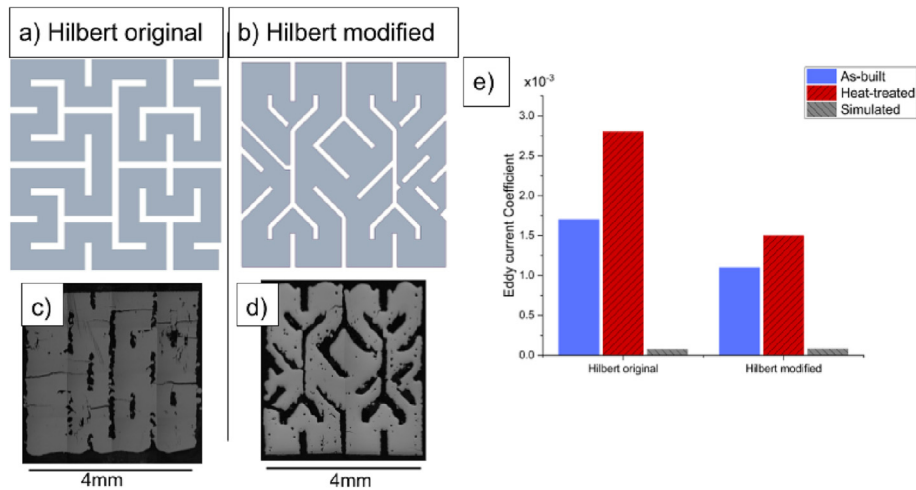


**Fig. 14.** Hilbert and the modified Hilbert cross sections, where the modified cross section has no surfaces which would overhang by more than 45°. Micrographs of these sections demonstrate that the modified Hilbert section is more similar to the intended design. The Hilbert section shows lower losses in the simulation, whilst the modified Hilbert section shows lower losses in the physical sample (e), due to a more accurate representation of the desired geometry.

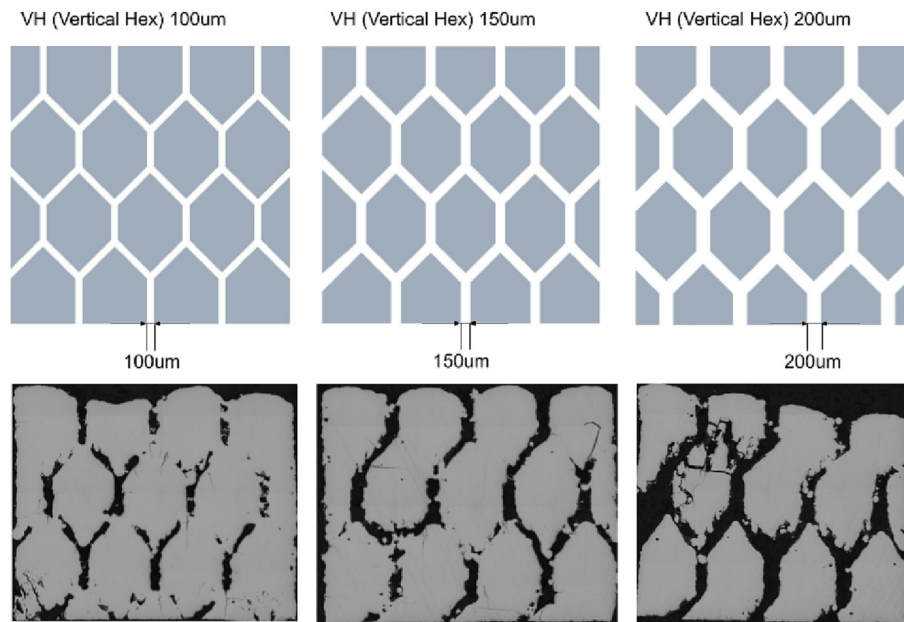


**Fig. 15.** Loss behaviour of hexagonal cross sections AB with differing air gaps and designs from Fig. 15. The lowest losses are for the HH section with 200  $\mu\text{m}$  gaps, as can be seen in Figure 15 this has the best electrical isolation between the different sections. The VH sections show the losses reducing with an increasing air gap size, however, this also reduces the SF from 87% to 74%.

Another method to reduce the likelihood of shorting between areas that should be electrically isolated by an air gap, is to increase the nominal width of the air gaps. By using a modified hexagonal section with no overhanging surfaces above 45° to the baseplate, the air gaps are modified in size as shown in Fig. 15. Increasing these air gaps has a positive effect on the loss behaviour as shown in Fig. 16, explained by reduced electrical shorting between areas that are supposed to be isolated, from 27% for the 100  $\mu\text{m}$  gap sample to only 0.5% for the 200  $\mu\text{m}$  gap sample. This does however have an undesirable effect on the SF. By increasing the air gaps the SF is reduced from 87% for the 100  $\mu\text{m}$  gap sample, to only 74% for the 200  $\mu\text{m}$  gap sample. It's also worth noting that for the 200  $\mu\text{m}$  sample, other build defects were more prevalent than the other samples, such as cracking or porosity. However,

there was very little electrical shorting observed. It appears that the support structures between the hexagons were not sufficient in the 200  $\mu\text{m}$  sample as the hexagons at the top are not in the correct position and appear to be slumping onto the ones below.

To better resolve the cross sections and decrease the air gap, the surface roughness of the builds could be improved. This would reduce the electrical shorting between areas that are intended to be insulated from each other by air but could also mean that the air gaps could be reduced in width, resulting in a higher SF. Improving the surface roughness may also improve the magnetic properties as the rough surface could act as pinning sites for magnetic domains, reducing the permeability and increasing the coercive force and losses. Post processing may also be used to improve this such as chemical polishing or electro-polishing.

#### 4. Conclusion

This paper demonstrates the ability of AM to process fully dense (greater than 99.5%) high silicon steel using L-PBF, with magnetic properties of  $H_c = 26$  A/m,  $\mu_{max} = 10,000$ , and  $B_{50} = 1.3$  T, sufficient to be useable in an EM. A novel hexagonal cross section was shown to significantly reduce the eddy current coefficient,  $C_{eddy}$ , from the bulk value of 0.0021 to 0.0005. Simulations were shown to correlate well with the bulk cross section, but physical samples with complex cross sections underperformed when compared to the simulations. The hexagonal section outperformed both the Hilbert and slotted cross sections previously produced in literature. Difficulties were found when trying to build the cross sections in three dimensions, which were shown to improve with modified cross sectional geometry to reduce horizontal overhanging surfaces. Electrical shorting between areas that should be insulated from each other was shown to be approximately 10% for the slotted cross section, yielding an order of magnitude decrease in performance from that predicted by simulations. By increasing the air gap the electrical shorting was improved from 27% to 0.5% in the 100  $\mu\text{m}$  and 200  $\mu\text{m}$  gap hexagonal samples respectively, with the 200  $\mu\text{m}$  gap sample being the closest to the simulated value at just under double the eddy current coefficient. Improvements in surface finish and accurate reproduction of the desired geometry are likely to give further performance benefits, which could be achieved with process parameter optimisation and/or post-processing, which will also aid in improving SF to higher than 90%. The eddy current loss coefficient  $C_{eddy}$  was shown to increase in all samples after HT, suggesting that the AB condition may give lower losses for high-frequency machines.

#### CRedit authorship contribution statement

**Alexander D. Goodall:** Conceptualization, Data curation, Formal analysis, Investigation, Methodology, Writing – original draft.

**Georgios Yiannakou:** Data curation, Methodology. **Lova Chechik:** Software, Writing – review & editing. **Ria L. Mitchell:** Data curation, Methodology. **Geraint W Jewell:** Data curation, Methodology. **Iain Todd:** Conceptualization, Data curation, Formal analysis, Methodology, Funding acquisition, Supervision, Writing – review & editing.

#### Data availability

Data will be made available on request.

#### Declaration of Competing Interest

The authors declare that they have no known competing financial interests or personal relationships that could have appeared to influence the work reported in this paper.

#### Acknowledgements

We wish to acknowledge the Henry Royce Institute for Advanced Materials, funded through EPSRC grants EP/R00661X/1, EP/S019367/1, EP/P02470X/1 and EP/P025285/1, for access to the AconityMini at The University of Sheffield. We also acknowledge Sheffield Tomography Centre and University of Sheffield funding from EPSRC (EP/T006390/1) for use of the Zeiss Xradia 620 Versa X-ray microscope. For the purpose of open access, the author has applied a Creative Commons Attribution (CC BY) licence to any Author Accepted Manuscript version arising.

#### Appendix A

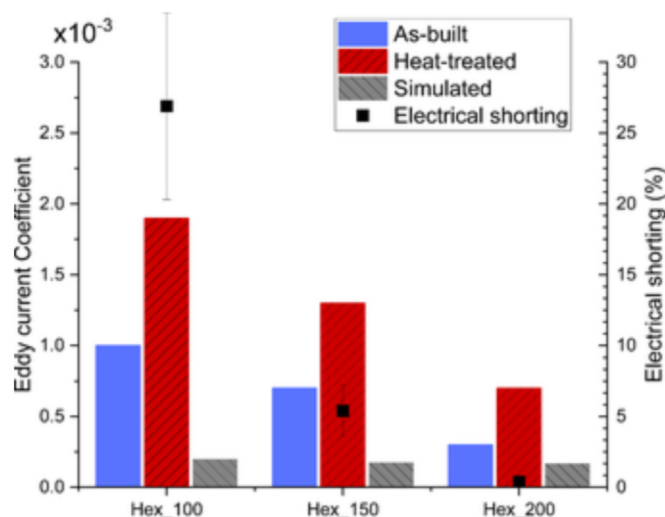


**Fig. 16.** Full size image showing solid cross section eddy current density with arrows to show current direction.

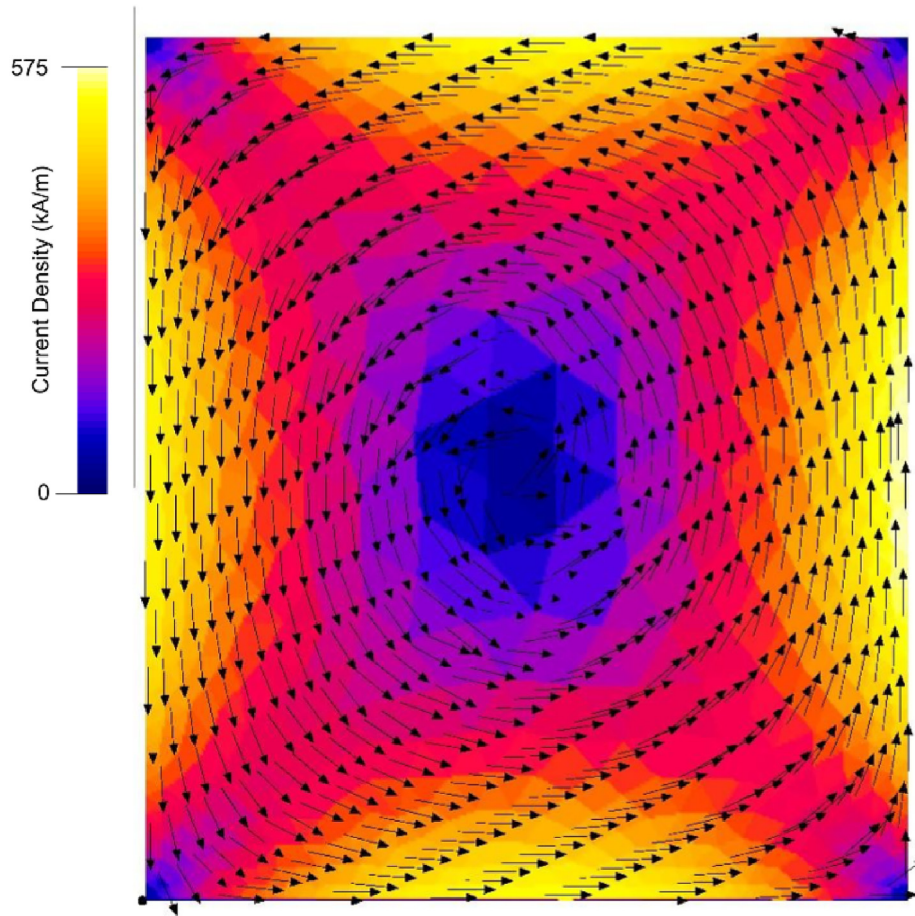


Fig. 17. Full size image showing hexagonal cross section eddy current density with arrows to show current direction, using a more suitable scale than Fig. 10.

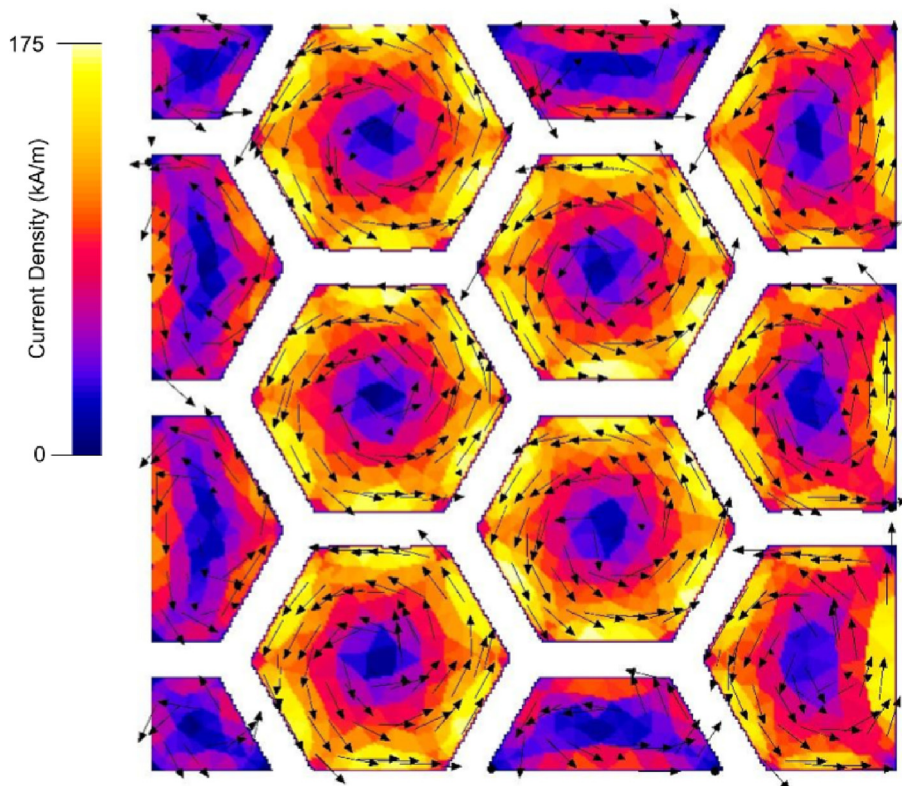


Fig. 18. Full size image showing slotted cross section eddy current density with arrows to show current direction, using a more suitable scale than Fig. 8.

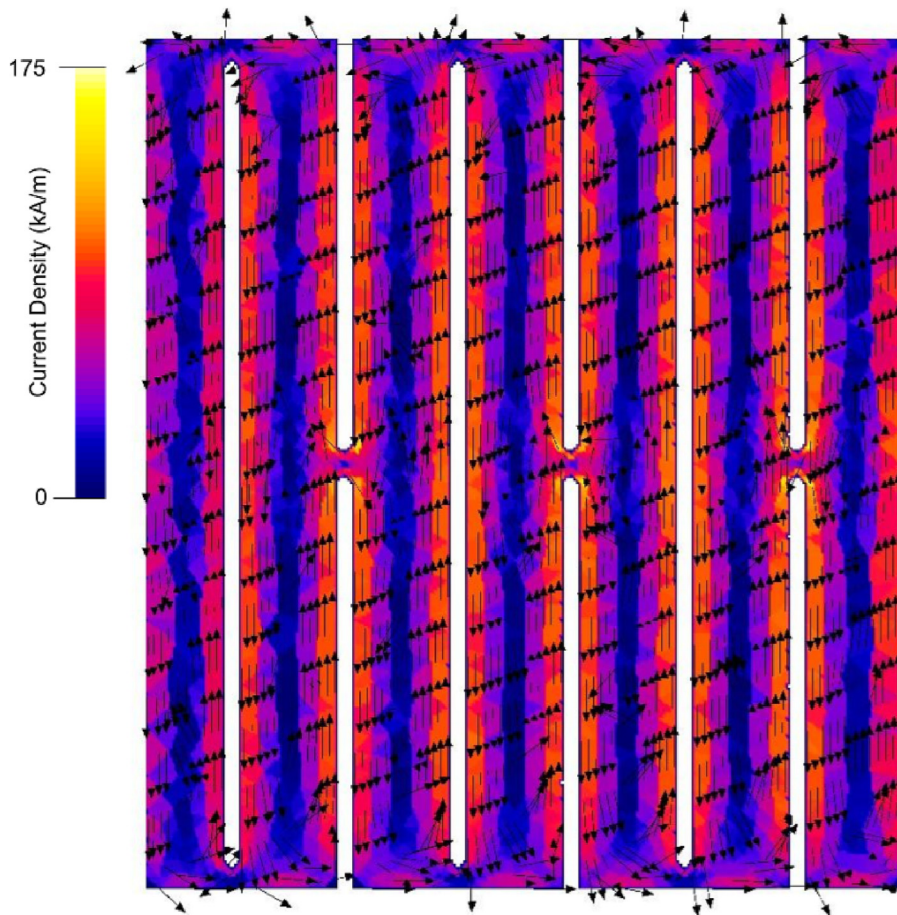


Fig. 19. Full size image showing Hilbert cross section eddy current density with arrows to show current direction, using a more suitable scale than Fig. 8.

## References

- [1] Wadie, Paul and Brunner, Conrad U, 'Energy-Efficiency Policy Opportunities for Electric Motor-Driven Systems', IEA Energy Papers 2011/07, May 2011. doi: 10.1787/5kgg52gb9gjd-en.
- [2] W. Cao, B.C. Mecrow, G.J. Atkinson, J.W. Bennett, D.J. Atkinson, Overview of electric motor technologies used for more electric aircraft (MEA), *IEEE Trans. Ind. Electron.* 59 (9) (Sep. 2012) 3523–3531, <https://doi.org/10.1109/TIE.2011.2165453>.
- [3] Z. Zhang, K. J. Jhong, C. Cheng, P. Huang, M. Tsai, and W. Lee, 'Metal 3D printing of synchronous reluctance motor', in *2016 IEEE International Conference on Industrial Technology (ICIT)*, Mar. 2016, pp. 1125–1128. doi: 10.1109/ICIT.2016.7474912.
- [4] P.-W. Huang, I.-H. Jiang, M.-C. Tsai, G.-M. Chen, New hybrid stator design for high-speed pmsms based on selective laser melting of 3-D printing, *IEEE Trans. Magn.* 55 (7) (2019) 1–4, <https://doi.org/10.1109/TMAG.2019.2901502>.
- [5] T.N. Lamichhane, L. Sethuraman, A. Dalagan, H. Wang, J. Keller, M.P. Paranthaman, Additive manufacturing of soft magnets for electrical machines—a review, *Mater. Today Phys.* 15 (2020), <https://doi.org/10.1016/j.mtphys.2020.100255> 100255.
- [6] Q. Jiang et al., 'A Review on Additive Manufacturing of Pure Copper', *Coatings*, vol. 11, no. 6, Art. no. 6, Jun. 2021, doi: 10.3390/coatings11060740.
- [7] M. Littmann, Iron and silicon-iron alloys, *IEEE Trans. Magn.* 7 (1) (1971) 48–60, <https://doi.org/10.1109/TMAG.1971.1066998>.
- [8] G. Ouyang, X. Chen, Y. Liang, C. Macziewski, J. Cui, Review of Fe-6.5 wt%Si high silicon steel—A promising soft magnetic material for sub-kHz application, *J. Magn. Mater.* 481 (2019) 234–250, <https://doi.org/10.1016/j.jmmm.2019.02.089>.
- [9] A. Krings, M. Cossale, A. Tenconi, J. Soulard, A. Cavagnino, A. Boglietti, Magnetic materials used in electrical machines: a comparison and selection guide for early machine design, *IEEE Ind. Appl. Mag.* 23 (6) (2017) 21–28, <https://doi.org/10.1109/MIAS.2016.2600721>.
- [10] D. Goll, J. Schurr, F. Trauter, J. Schanz, T. Bernthaler, H. Riegel, G. Schneider, Additive manufacturing of soft and hard magnetic materials, *Procedia CIRP* 94 (2020) 248–253.
- [11] A. Plotkowski, J. Pries, F. List, P. Nandwana, B. Stump, K. Carver, R.R. Dehoff, Influence of scan pattern and geometry on the microstructure and soft-magnetic performance of additively manufactured Fe-Si, *Addit. Manuf.* 29 (2019) 100781.
- [12] F.S.H.B. Freeman, A. Lincoln, J. Sharp, A. Lambourne, I. Todd, Exploiting thermal strain to achieve an in-situ magnetically graded material, *Mater. Des.* 161 (Jan. 2019) 14–21, <https://doi.org/10.1016/j.matdes.2018.11.011>.
- [13] M. Yakout, M. A. Elbestawi, L. Wang, and R. Muizelaar, 'Selective laser melting of soft magnetic alloys for automotive applications', p. 4, Sep. 2019.
- [14] H. Tiismus et al., 'AC Magnetic Loss Reduction of SLM Processed Fe-Si for Additive Manufacturing of Electrical Machines', *Energies*, vol. 14, no. 5, Art. no. 5, Jan. 2021, doi: 10.3390/en14051241.
- [15] Z. Strecker, M. Kubík, P. Vítek, J. Roupec, D. Paloušek, V. Šreibr, Structured magnetic circuit for magnetorheological damper made by selective laser melting technology, *Smart Mater. Struct.* 28 (5) (2019), <https://doi.org/10.1088/1361-665X/ab0b8e> 055016.
- [16] M. Garibaldi, I. Ashcroft, M. Simonelli, R. Hague, Metallurgy of high-silicon steel parts produced using Selective Laser Melting, *Acta Mater.* 110, no. C (2016) 207–216, <https://doi.org/10.1016/j.actamat.2016.03.037>.
- [17] M. Garibaldi, I. Ashcroft, N. Hillier, S.A.C. Harmon, R. Hague, Relationship between laser energy input, microstructures and magnetic properties of selective laser melted Fe-6.9wt% Si soft magnets, *Mater. Charact.* 143 (Sep. 2018) 144–151, <https://doi.org/10.1016/j.matchar.2018.01.016>.
- [18] J.N. Lemke, M. Simonelli, M. Garibaldi, I. Ashcroft, R. Hague, M. Vedani, R. Wildman, C. Tuck, Calorimetric study and microstructure analysis of the order-disorder phase transformation in silicon steel built by SLM, *J. Alloys Compd.* 722 (2017) 293–301.
- [19] T. Q. Pham, T. T. Do, P. Kwon, and S. N. Foster, 'Additive Manufacturing of High Performance Ferromagnetic Materials', in *2018 IEEE Energy Conversion Congress and Exposition (ECCE)*, Sep. 2018, pp. 4303–4308. doi: 10.1109/ECCE.2018.8558245.
- [20] H. Tiismus, A. Kallaste, A. Rassölin, T. Vaimann, Preliminary analysis of soft magnetic material properties for additive manufacturing of electrical machines, *Key Eng. Mater.* 799 (2019) 270–275, <https://doi.org/10.4028/www.scientific.net/KEM.799.270>.
- [21] S. Yamaura, Y. Furuya, T. Watanabe, The effect of grain boundary microstructure on Barkhausen noise in ferromagnetic materials, *Acta Mater.* 49 (15) (Sep. 2001) 3019–3027, [https://doi.org/10.1016/S1359-6454\(01\)00189-6](https://doi.org/10.1016/S1359-6454(01)00189-6).

- [22] B. Zhang, N.-E. Fenineche, H. Liao, C. Coddet, Magnetic properties of in-situ synthesized FeNi<sub>3</sub> by selective laser melting Fe-80%Ni powders, *J. Magn. Mater.* 336 (2013) 49–54, <https://doi.org/10.1016/j.jmmm.2013.02.014>.
- [23] C.A. Schneider, W.S. Rasband, K.W. Eliceiri, NIH image to ImageJ: 25 years of image analysis, *Nat. Methods* 9 (7) (2012) 671–675.
- [24] 'BS 60404-4 DC measurements'. <https://bsol-bsigroup-com.sheffield.idm.oclc.org/Bibliographic/BibliographicInfoData/00000000030313864> (accessed Jan. 14, 2021).
- [25] S. Tumanski, *Handbook of Magnetic Measurements*, CRC Press, 2016.
- [26] M. Garibaldi, I. Ashcroft, J.N. Lemke, M. Simonelli, R. Hague, Effect of annealing on the microstructure and magnetic properties of soft magnetic Fe-Si produced via laser additive manufacturing, *Scr. Mater.* 142 (2018) 121–125, <https://doi.org/10.1016/j.scriptamat.2017.08.042>.
- [27] B.D. Cullity, C.D. Graham, *Introduction to Magnetic Materials*, John Wiley & Sons, 2011.
- [28] M. Garibaldi, C. Gerada, I. Ashcroft, and R. Hague, 'Free-Form Design of Electrical Machine Rotor Cores for Production Using Additive Manufacturing', *J. Mech. Des.*, vol. 141, no. 7, Jul. 2019, doi: 10.1115/1.4042621.